Inorganic Chemistry

Article

pubs.acs.org/IC

Role of Noncovalent Interactions in Vanadium Tellurite Chain Connectivities

Anahita Nourmahnad,[†] Matthew D. Smith,[†] Matthias Zeller,[‡] Gregory M. Ferrence,[§] Joshua Schrier,[†] and Alexander J. Norquist*[,†]

[†]Department of Chemistry, Haverford College, Haverford, Pennsylvania 19041, United States

[‡]Department of Chemistry, Youngstown State University, Youngstown, Ohio 44555, United States

[§]Department of Chemistry, Illinois State University, Normal, Illinois 61790, United States

Supporting Information

ABSTRACT: Structural differences in $[V_2Te_2O_{10}]_n^{2n-}$ chain metrics are directly ascribed to variations in noncovalent interactions in a series of organically templated vanadium tellurites, including $[C_6H_{17}N_3][V_2Te_2O_{10}]\cdot H_2O$, $[C_5H_{16}N_2][V_2Te_2O_{10}]$, and $[C_4H_{14}N_2][V_2Te_2O_{10}]$. The noncovalent interaction (NCI) method was used to locate, quantify, and visualize intermolecular interactions in $[C_4H_{14}N_2][V_2Te_2O_{10}]$ and $[C_5H_{16}N_2][V_2Te_2O_{10}]$. Variations in the van der Waals attractions between $[1,4\text{-diaminobutaneH}_2]^{2+}$ and $[1,5\text{-diaminopentaneH}_2]^{2+}$ result in divergent packing motifs for these cations, which causes a reorganization of N−H···O hydrogen bonding and variances in the $[V_2Te_2O_{10}]_n^{2n-}$ chain metrics. The application of the NCI method to this type of solid-state structure provides a direct method to elucidate the structural effects of weak noncovalent interactions.

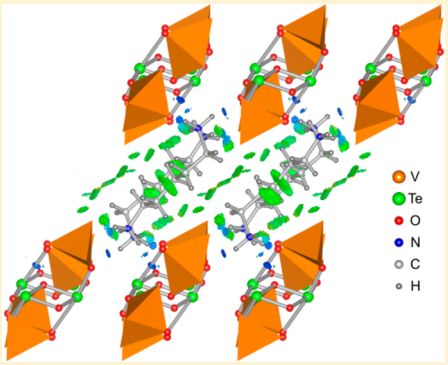

INTRODUCTION

The chemistry of inorganic−organic hybrid materials has been the focus of intense interest for decades because of their wide range of technologically advantageous properties, astounding compositional breadth, and exceptional diversity of structure. Example families of these compounds include metal−organic frameworks,[1−3] supramolecular compounds,[4−7] and organically templated metal oxides.[8,9] The bonding in these materials is just as diverse as their structures, with covalent, ionic, and coordination bonds, hydrogen bonding, van der Waals forces, and $\pi-\pi$ stacking being observed in a single compound.

Structural analyses of inorganic−organic hybrid materials tend to focus on covalent, ionic, and coordination bonds because such interactions are easily identified and quantified using the heavy atom positions obtained from X-ray diffraction experiments. Similarly, O/N−H···O hydrogen bonds typically can be defined by anion−anion distances, and the range of observed angles is small. In contrast, the contributions and effects of weaker attractions, such as C−H···O hydrogen bonds, van der Waals forces, and $\pi-\pi$ stacking, are more difficult to quantify because of the lack of an easily observable structural proxy for strength and a greater uncertainty of the hydrogen atom positions. However, these interactions are ubiquitous in inorganic−organic hybrid materials and can exert considerable influence over structure. For example, Desiraju et al. have clearly demonstrated the importance of C−H···O hydrogen bonds in a range of systems.[10−13] Assigning structural effects to these weaker interactions can pose a challenge during structural analyses.

The focus of this Article is the role of weak noncovalent interactions in organically templated metal oxides. On the basis of the experimentally determined crystal structures, noncovalent interactions (NCI)[14,15] were calculated for a series of organically templated vanadium tellurites. NCI analysis uses qualitative density functional theory and relies on the observation that noncovalent interactions occur in regions where the electron density, ρ, and its first derivative, specifically, the reduced density gradient, are small. The reduced density gradient is represented as

$$s = \frac{|\nabla\rho|}{2(3\pi^2)^{1/3}\rho^{4/3}} \quad (1)$$

Although NCI calculations have been extensively applied to gas-phase molecular interactions,[15,16] the application of this method to solids[15] is more recent. The applications of this method to solids have focused primarily on organic molecular crystals[17,18] and alkali metal coordination complexes.[19] To our knowledge, the only previous application to inorganic chemistry has been work by Mellot-Draznieks and co-workers on zeolitic imidazolate frameworks (ZIFs).[20] In previous work, it has been found that the sign of the second eigenvalue, λ_2, of the electron-density Hessian (second-derivative) matrix distinguishes between attractive ($\lambda_2 < 0$) and repulsive ($\lambda_2 > 0$) regions[14] and that the total electron density contained within a particular region of space semiquantitatively describes the strength of the

Received: November 14, 2014
Published: January 8, 2015

DOI: 10.1021/ic502753e
Inorg. Chem. 2015, 54, 694−703

interaction.[15] These NCI calculations allow for the location, quantification, and visualization of individual N−H···O and C−H···O hydrogen bonds and weak ionic and van der Waals interactions. In this Article, we present the use of this computational technique to understand subtle structural differences in a series of organically templated vanadium tellurites that contain a $[V_2Te_2O_{10}]_n^{2n-}$ chain. We are able to attribute specific structural differences in $[C_6H_{17}N_3][V_2Te_2O_{10}]\cdot H_2O$ (**1**), $[C_5H_{16}N_2][V_2Te_2O_{10}]$ (**2**), and $[C_4H_{14}N_2][V_2Te_2O_{10}]$[21] to the interactions identified using the NCI method.

EXPERIMENTAL SECTION

Materials. NH_4VO_3 (99.99%), Na_2TeO_3 (99.5%), 1-(2-aminoethyl)piperazine (aep, 99%), and 1,5-diaminopentane (1,5-dap, 97%) were purchased from Aldrich and used as received. Deionized water was used in these syntheses.

Synthesis. All reactions were conducted in 23 mL poly(fluoroethylene-propylene)-lined pressure vessels. The pH values of the initial reaction mixtures were adjusted to 8 using 2 M HCl. Reaction mixtures were heated to 90 °C and allowed to soak for 24 h. The reactions were then cooled to room temperature at a rate of 6 °C h^{-1} to promote the growth of large single crystals. Autoclaves were opened in air, and the products were recovered through filtration. No additional crystalline or amorphous reaction products were observed.

$[C_6H_{17}N_3][V_2Te_2O_{10}]\cdot H_2O$ (1). Compound **1** was synthesized as single crystals through the reaction of 0.2011 g (1.72×10^{-3} mol) of NH_4VO_3, 0.2223 g (1.05×10^{-3} mol) of Na_2TeO_3, 0.1238 g (9.98×10^{-4} mol) of aep, and 8.9400 g (4.97×10^{-1} mol) of water. Yellow blocks were produced in 32.4% yield (based upon Te). IR data (cm^{-1}): N−H, 1443, 1494, 1580; C−H, 3088; Te−O, 742; Te−O−Te, 424, 649; V−O, 914. Elemental analysis observed % (calcd %): C 11.00 (10.81), H 2.85 (2.90), N 6.31 (6.30).

$[C_5H_{16}N_2][V_2Te_2O_{10}]$ (2). Compound **2** was synthesized as single crystals through the reaction of 0.1493 g (1.28×10^{-3} mol) of NH_4VO_3, 0.1391 g (6.57×10^{-4} mol) of Na_2TeO_3, 0.0612 g (6.00×10^{-4} mol) of 1,5-dap, and 9.0059 g (5.00×10^{-1} mol) of water. Yellow blocks were produced in 40.68% yield (based upon Te). IR data (cm^{-1}): N−H, 1484, 1520, 1588; C−H, 2862; Te−O, 737; Te−O−Te, 450, 689; V−O, 886. Elemental analysis observed % (calcd %): C 9.68 (9.74), H 2.41 (2.42), N 4.44 (4.42).

Single-Crystal X-ray Diffraction. Data were collected using a Bruker AXS Smart Apex or an Apex II CCD diffractometer with Mo Kα radiation (λ = 0.71073 Å). A single crystal was mounted on a Mitegen micromesh mount using a trace amount of mineral oil and cooled in situ to 100(2) K for data collection. Frames were collected; reflections were indexed and processed, and the files were scaled and corrected for absorption using APEX2.[22] The heavy atom positions were determined using SIR92.[23] All other non-hydrogen sites were located from Fourier difference maps. All non-hydrogen sites were refined using anisotropic thermal parameters using full-matrix least-squares procedures on F_o^2 with $I > 3\sigma(I)$. Hydrogen atoms were placed in geometrically idealized positions. All calculations were carried out using Crystals, version 14.23c.[24] Relevant crystallographic data are listed in Table 1. Crystallographic disorder within the organic component in **1** was modeled using 50% occupancies for O6, N1, C1, C2, C4, C5, H1−H6, and H9−H17.

Powder X-ray Diffraction. Powder diffraction patterns were recorded on a GBC-Difftech MMA powder diffractometer. Dry powdered samples were packed into sample holders. Samples were mounted on glass plates. Calculated powder patterns were generated from single-crystal data using ATOMS, version 6.0.[25] Powder X-ray diffraction patterns were consistent with those predicted from the refined structures of **1** and **2**. No evidence of additional phases was observed.

Infrared Spectroscopy. Infrared measurements were recorded using a PerkinElmer FT-IR Spectrum 1000 spectrophotometer. Samples were diluted with spectroscopic grade KBr and pressed into pellets. Scans were collected over the range of 400−4000 cm^{-1}.

Table 1. Crystallographic Data for Compounds $[C_6H_{17}N_3][V_2Te_2O_{10}]\cdot H_2O$ (1) and $[C_5H_{16}N_2][V_2Te_2O_{10}]$ (2)

compound	$[C_6H_{17}N_3][V_2Te_2O_{10}]\cdot H_2O$ (**1**)	$[C_5H_{16}N_2][V_2Te_2O_{10}]$ (**2**)
formula	$C_6H_{19}N_3O_{11}Te_2V_2$	$C_5H_{16}N_2O_{10}Te_2V_2$
fw	666.31	621.27
space group	*C*2/*c* (No. 15)	*P*-1 (No. 2)
a (Å)	25.42(3)	7.5506(3)
b (Å)	5.759(8)	8.9255(4)
c (Å)	12.008(16)	11.4699(5)
α (deg)	90	93.4986(16)
β (deg)	107.141(16)	93.7112(15)
γ (deg)	90	96.8662(15)
V (Å^3)	1680(4)	763.99(3)
Z	4	2
ρ_{calc} (g cm^{-3})	2.634	2.701
λ (Å)	0.71073	0.71073
T (K)	100	100
μ (mm^{-1})	4.575	5.014
$R_1{}^a$	0.0414	0.0126
$wR_2{}^b$	0.0973	0.0375

$^aR_1 = \sum||F_o| - |F_c||/\sum|F_o|$. $^bwR_2 = [\sum w(F_o^2 - F_c^2)^2]/[\sum w(F_o^2)^2]^{1/2}$.

Bond Valence Sums. The hydrogen-bonding networks present in compounds **1** and **2** were analyzed using bond valence sums.[26] All calculations were carried out using parameters compiled by Brese and O'Keeffe.[27] Complete tables of bond valence sums for each compound are available in the Supporting Information.

Electronic Structure Calculations. Solid-state electronic structure calculations were carried out using ABINIT, version 6.4.1.[28,29] ABINIT calculations used the Perdew−Burke−Ernzerhof generalized gradient approximation (PBE-GGA) exchange-correlation functional, norm-conserving Troullier−Martins pseudopotentials, a planewave basis set with an energy cutoff of 25 hartree, a 6 × 6 × 6 Monkhorst−Pack k-point sampling grid, and experimental crystal structures. Electron localization functions (ELFs) were calculated from the self-consistent valence electron densities and visualized using Vesta, version 3.1.7.[30]

Noncovalent Interaction (NCI) Index Calculations. NCI analyses were carried out using CRITIC 2, version 1.0,[31,32] to generate promolecular densities using the default numerical free atom densities. The spatial distribution of a particular interaction can be described in terms of a region in space, Ω(NCI), that is defined by the values and upper bound of *s* and a range of sign $(\lambda_2)\rho$. Plotting the isosurface defined by these bounds shows the spatial location of the interaction; coloring of the isosurface, as a function of the sign $(\lambda_2)\rho$ value, indicates the qualitative strength of the interaction.[33] A semiquantitative estimate of the interaction energy can be determined by integrating

$$q = \int_{\Omega(\mathrm{NCI})} \rho^n(\vec{r})\, \mathrm{d}\vec{r} \qquad (2)$$

where $n = {}^4/_3$ is an empirical constant that was identified as giving the best agreement between the MP2 calculations of hydrogen bonds and the NCI interaction energy. Values of n = 1, ${}^5/_3$, and 2 also give qualitatively similar results. Ratios of q for the two structures were calculated to show the relative strengths of the interactions at play either between the two structures or within a given structure. Interaction types (ionic, hydrogen bonding, or van der Waals) were identified through the extraction of isosurfaces for each peak. The integrations were carried out numerically by integration over a cubic grid with 0.1 au increments. The extraction of isosurfaces corresponding to particular interactions and the integration of interaction strengths were carried out using Mathematica, version 10.0.0.0 (Supporting Information), and visualized using Vesta, version 3.1.7.

DOI: 10.1021/ic502753e
Inorg. Chem. 2015, 54, 694−703

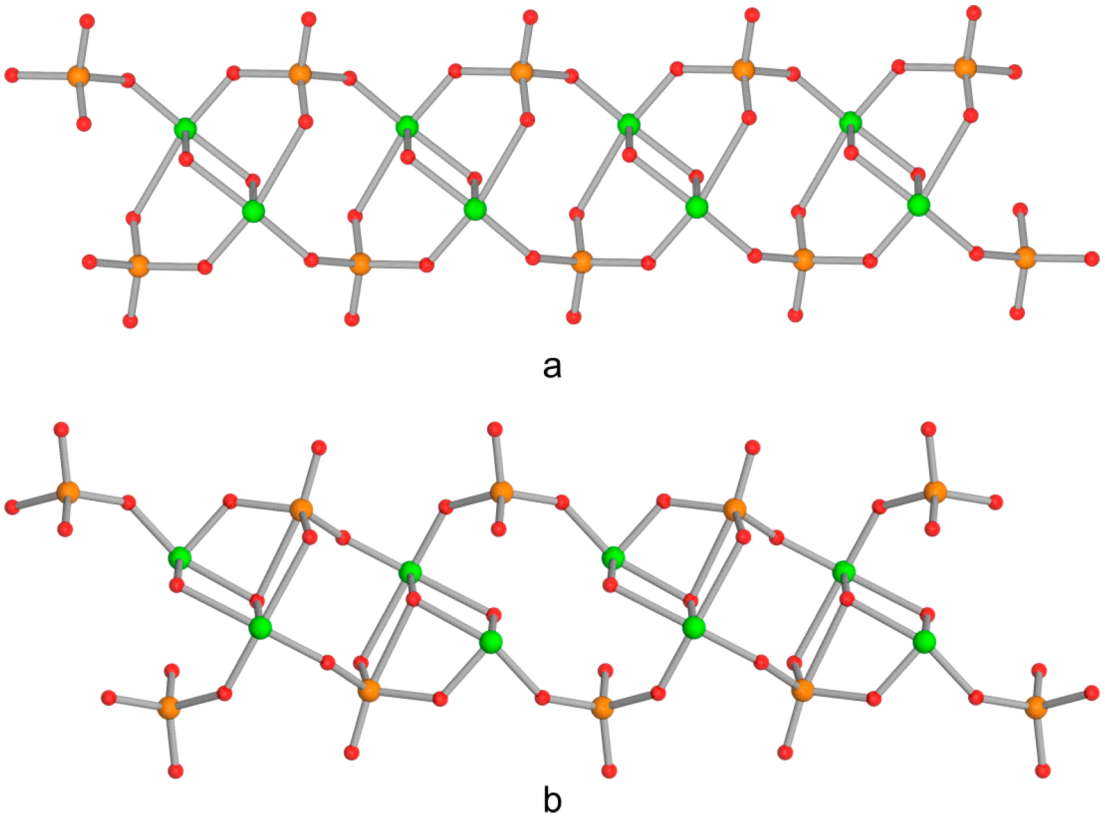

Figure 1. $[V_2Te_2O_{10}]_n^{2n-}$ chain connectivities in (a) $[C_4H_{14}N_2][V_2Te_2O_{10}]$ and **1** and (b) **2**. Orange, green, and red spheres represent vanadium, tellurium, and oxygen, respectively.

RESULTS

Compound **1** contains one vanadium site, in the form of a $[VO_4]$ tetrahedron. A single $V-O_{terminal}$ bond is observed, with a length of 1.630(6) Å, whereas the $V-O_{bridging}$ distances span 1.661(5)–1.846(5) Å. $[Te_2O_8]$ dimers are present in **1**, with Te–O distances of 1.895(5)–2.710(6) Å. All vanadium and tellurium centers are formally V^{5+} and Te^{4+}, respectively. The $[Te_2O_8]$ dimers are connected to the $[VO_4]$ tetrahedra, forming $[V_2Te_2O_{10}]_n^{2n-}$ chains that are isotypic of those observed in $[C_4H_{14}N_2][V_2Te_2O_{10}]$ (Figure 1).[21]

Compound **2** contains both $[VO_4]$ and $[VO_5]$ environments, with $V-O_{terminal}$ bond lengths of 1.6343(13) and 1.6400(12) Å, respectively. The $V-O_{bridging}$ distances are generally longer, with distances between 1.6483(12) and 2.5814(12) Å. $[Te_2O_7]$ dimers are present in **2**, with Te–O distances of 1.8678(11)–2.6077(12) Å. All vanadium and tellurium centers are formally V^{5+} and Te^{4+}, respectively. The $[Te_2O_7]$ dimers in **2** are also connected to the $[VO_4]$ and $[VO_5]$ polyhedra to form related $[V_2Te_2O_{10}]_n^{2n-}$ chains (Figure 1). The bonding networks in **1** and **2** were probed using bond valence sums.[26,27] The calculated $\sum S_i$ values for each cation correspond to their formal oxidation states, with vanadium and tellurium values of 4.96–5.03 vu and 3.95–4.15 vu, respectively. Full tables of bond valence sums for **1** and **2** are available in the Supporting Information.

The $[V_2Te_2O_{10}]_n^{2n-}$ chains in **1** and **2** are related to those in another recently reported compound, $[C_4H_{14}N_2][V_2Te_2O_{10}]$.[21] The $[V_2Te_2O_{10}]_n^{2n-}$ chains in **1** are directly analogous to the chains in $[C_4H_{14}N_2][V_2Te_2O_{10}]$, whereas distortions in the $[V_2Te_2O_{10}]_n^{2n-}$ chains in **2** result in a related but distinctly different chain connectivity. Selected interatomic distances are provided in Figure 2, whereas complete tables of bond distances are available in CIF format in the Supporting Information. The bonding metrics in **1** and $[C_4H_{14}N_2][V_2Te_2O_{10}]$ (Figure 2a,b, respectively) are nearly identical, and the $[V_2Te_2O_{10}]_n^{2n-}$ chains in both of these compounds are constructed from $[VO_4]$ tetrahedra and $[Te_2O_8]$ dimers. In contrast, the $[V_2Te_2O_{10}]_n^{2n-}$ chains in **2** contain $[VO_4]$ and $[VO_5]$ polyhedra and $[Te_2O_7]$ dimers.

The differences between the two chain connectivities shown in Figure 1 are manifested most directly in two specific interactions. First, a long fifth V–O bond is observed in the $[V(1)O_5]$ polyhedron in **2**, with a distance of 2.5814(12) Å and a bond valence of 0.12 vu (Figure 2c). This longer interaction is above the minimal value for a trans bond to V^{5+} defined by Schindler et al.[34] Analogous interactions in **1** and $[C_4H_{14}N_2][V_2Te_2O_{10}]$ have distances of 3.213(3) and 3.129(3) Å, respectively. The valences of these longer interactions (0.02 and 0.03 vu, respectively) are greatly reduced relative to that of **2** and are well below Schindler's minimal value, resulting in tetrahedral coordination designations for V1 in **1** and $[C_4H_{14}N_2][V_2Te_2O_{10}]$. Second, each Te^{4+} center in **1** and $[C_4H_{14}N_2][V_2Te_2O_{10}]$ has one long bonding interaction, with distances of 2.710(6) and 2.694(2) Å, respectively, and bond valences of 0.14 and 0.14 vu, respectively. Two distinct Te^{4+} sites are observed in **2**. Te2 is similar to the Te^{4+} sites in **1** and $[C_4H_{14}N_2][V_2Te_2O_{10}]$ because it has a similar long bonding interaction with a distance of 2.6077(12) Å. Te1, however, is distinctly different: the length of this long interaction is greatly increased to 3.0012(11) Å. The valences of these Te–O interactions in **2** are 0.18 and 0.06 vu, respectively.

Despite the differences among the $[V_2Te_2O_{10}]_n^{2n-}$ chains, the 3D packings of these structures are similar. The tellurite stereoactive lone pairs are oriented roughly perpendicular to the directions of chain propagation, forming pseudolayers of

DOI: 10.1021/ic502753e
Inorg. Chem. 2015, 54, 694–703

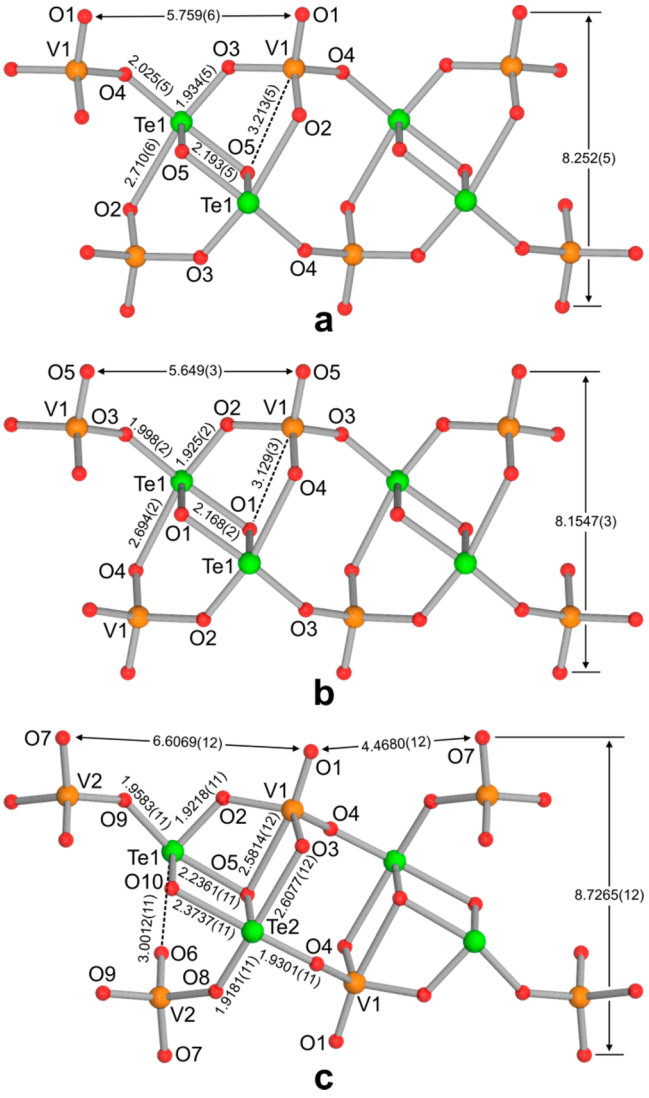

Figure 2. Ball-and-stick representations of the $[V_2Te_2O_{10}]_n^{2n-}$ chains in (a) **1**, (b) $[C_4H_{14}N_2][V_2Te_2O_{10}]$, and (c) **2**. Orange, green, and red spheres represent vanadium, tellurium, and oxygen, respectively. Selected distances are shown in angstroms.

$[V_2Te_2O_{10}]_n^{2n-}$ chains. Also, organic ammonium cations reside between the pseudolayers, creating an extensive hydrogen-bonding network. 3D packing figures for **1**, **2**, and $[C_4H_{14}N_2][V_2Te_2O_{10}]$ are shown in Figures 3, 4, and 5, respectively.

The strengths of the hydrogen-bond donors in these compounds are largely dictated by pK_a, whereas relative acceptor strengths can be determined using bond valence sums. The most underbonded oxide anions act as preferential hydrogen-bond acceptors. Such behavior has been observed in a range of systems.[35−42] Crystallographic disorder is observed in the $[aepH_2]^{2+}$ cations in **1**. Two $[aepH_2]^{2+}$ cations are superimposed over each cation position at a 1:1 ratio. The disordered $[aepH_2]^{2+}$ cations sit on 2-fold axes of rotation, constraining the populations of the two orientations to a ratio of 50:50. The specific orientation of each cation is randomly distributed. Views of the $[aepH_2]^{2+}$ disorder mechanism are provided in the Supporting Information.

NCI calculation results are shown in Figures 6−11. Plots of the reduced density gradient (s) versus sign (λ_2)ρ are shown in Figures 6 and 7, providing fingerprints that illustrate the types of

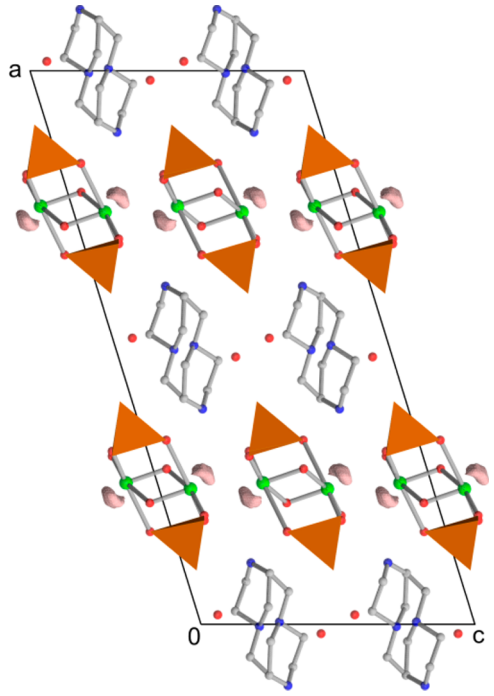

Figure 3. 3D packing of **1**. Orange polyhedra represent $[VO_4]$, whereas green, red, blue, and white spheres represent tellurium, oxygen, nitrogen, and carbon, respectively. ELF isosurfaces are shown with a boundary condition of 0.96. Hydrogen atoms have been omitted for clarity.

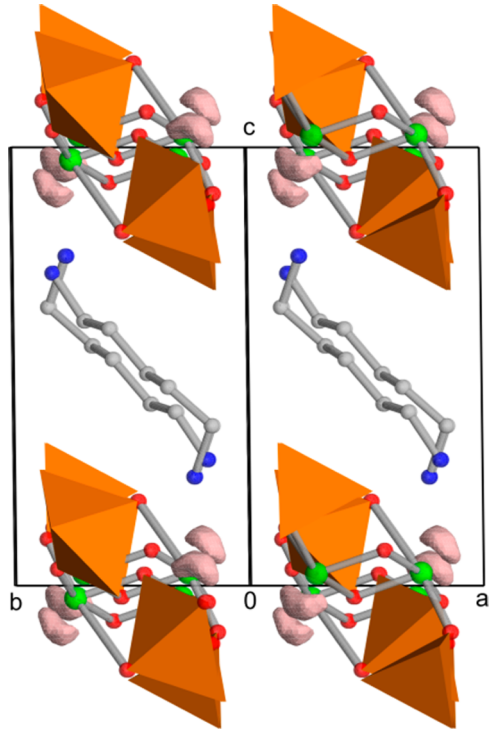

Figure 4. 3D packing of **2**. Orange polyhedra represent $[VO_4]$ and $[VO_5]$, whereas green, red, blue, and white spheres represent tellurium, oxygen, nitrogen, and carbon, respectively. ELF isosurfaces are shown with a boundary condition of 0.96. Hydrogen atoms have been omitted for clarity.

noncovalent interactions present. The identities of the different interactions, indicated by the symbols annotating Figures 6c and

DOI: 10.1021/ic502753e
Inorg. Chem. 2015, 54, 694−703

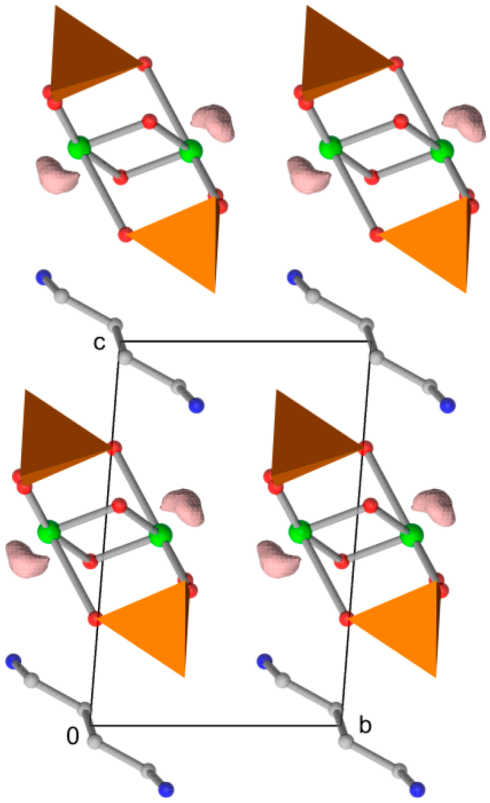

Figure 5. 3D packing of $[C_4H_{14}N_2][V_2Te_2O_{10}]$. Orange polyhedra represent $[VO_4]$, whereas green, red, blue, and white spheres represent tellurium, oxygen, nitrogen, and carbon, respectively. ELF isosurfaces are shown with a boundary condition of 0.96. Hydrogen atoms have been omitted for clarity.

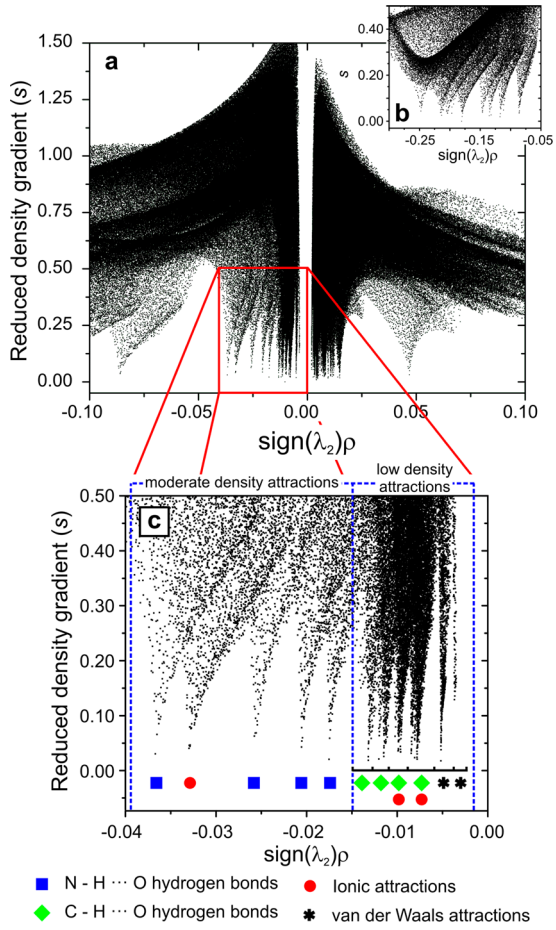

Figure 6. NCI analysis of $[C_4H_{14}N_2][V_2Te_2O_{10}]$, showing (a) both moderate- and low-density attractions and repulsions, (b) high-density attractions, and (c) an expanded view of the moderate- and low-density attractions.

7c, were determined by visualizing the regions of space, Ω(NCI), that are occupied by each peak. Ratios of relative interaction energies between $[C_4H_{14}N_2][V_2Te_2O_{10}]$ and **2** are shown in Figures 8 and 9. These ratios were calculated for different types of noncovalent interactions: moderate densities correspond to strong hydrogen bonds and weak ionic bonds, and low densities correspond to weak hydrogen bonds and dispersion interactions. The cutoffs used to distinguish between moderate- and low-density attractions are shown as blue dashed lines in Figures 6 and 7. The repulsive interactions correspond to sign $(\lambda_2)\rho > 0$. The ratio of the moderate- to low-density interactions within each of the structures is shown in Figure 10.

DISCUSSION

One must understand the influences that govern both the connectivities and compositions of the compounds discussed here to understand their structures and chemistry. During the past several years, we have published a series of Articles in which a hierarchy of influences that affect the outcome of hydrothermal reactions is described. The effects of these influences are not equal, and not all of them are present in each reaction. However, their elucidation is an important step toward understanding the formation of organically templated metal oxides. The primary influence on these reactions is the relative concentration of each reactive species. The identities of the reactive species are clearly affected by a range of experimental parameters, including pH, temperature-dependent metal speciation and differences associated with source materials and reaction times. In addition, the relative concentrations of reactants are well-known for directly affecting the identity and availability of the primary building units of which the larger structures are composed.[43−46] We have explored and observed the influence of reactant concentrations in a variety of systems.[38,41,47−50] The secondary influence on these reactions is charge-density matching[51,52] between the inorganic−anionic and organic−cationic components of these reactions. Although the charge densities of the organic cations are largely fixed by solution pH because it dictates their protonation states, the inorganic components can access a range of charge densities through the formation of different secondary building units (SBUs).[21,37,41] It is thought that charge-density matching between the cationic and anionic components is necessary for condensation and crystallization.[30,31] The primary and secondary influences largely determine the building blocks that form these crystalline solids; however, this fact neither addresses how the SBUs interact with one another, nor does it help us understand differences in local bonding metrics or symmetries in related systems.

Several tertiary influences are observed in the formation of organically templated metal oxides. These influences are generally weaker and do not dictate the compositions of the compounds or the nature of their respective SBUs. Instead, tertiary influences are involved in the interactions between the SBUs or between the inorganic−anionic and organic−cationic components. For example, we have described how hydrogen-bonding interactions between the protonated organic amines

DOI: 10.1021/ic502753e
Inorg. Chem. 2015, 54, 694−703

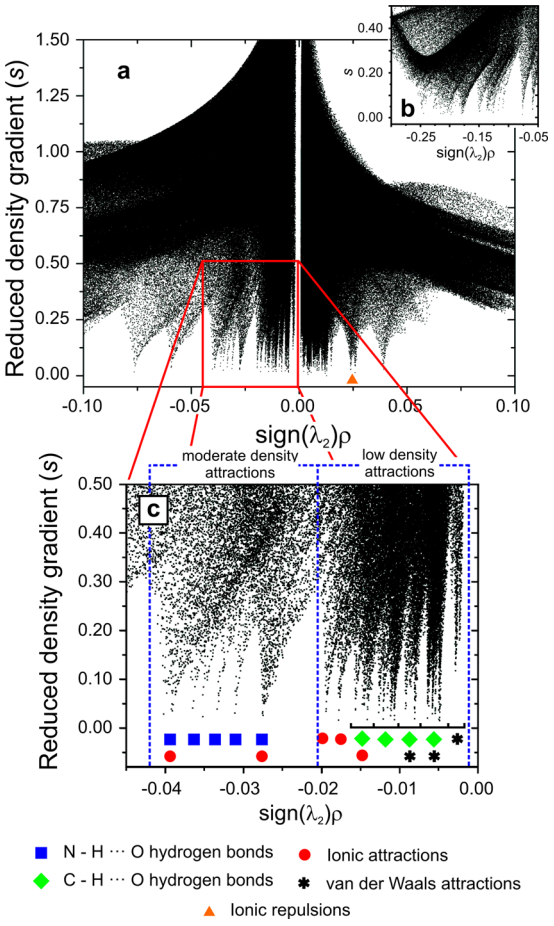

Figure 7. NCI analysis of $[C_5H_{16}N_2][V_2Te_2O_{10}]$ (**2**) showing (a) both moderate- and low-density attractions and repulsions, (b) high-density attractions, and (c) an expanded view of the moderate- and low-density attractions.

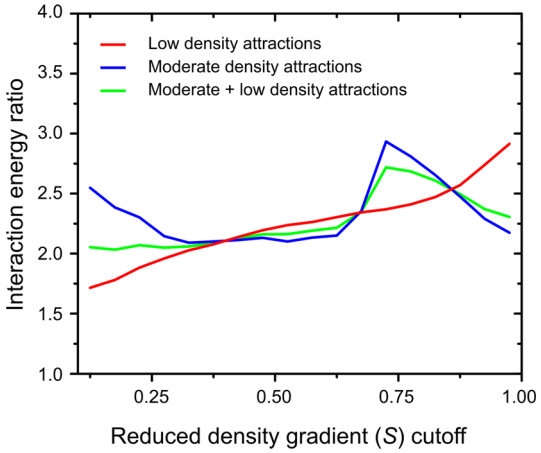

Figure 8. Attractive interaction energy ratios as a function of reduced density gradient cutoff for $[C_5H_{16}N_2][V_2Te_2O_{10}]$ (**2**)/$[C_4H_{14}N_2]$-$[V_2Te_2O_{10}]$.

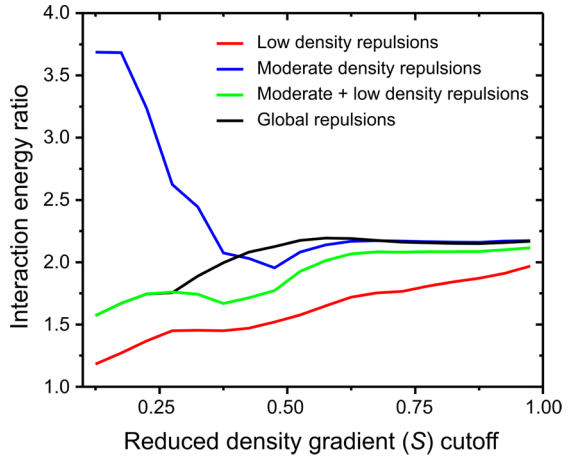

Figure 9. Repulsive interaction energy ratios as a function of reduced density gradient cutoff for $[C_5H_{16}N_2][V_2Te_2O_{10}]$ (**2**)/$[C_4H_{14}N_2]$-$[V_2Te_2O_{10}]$.

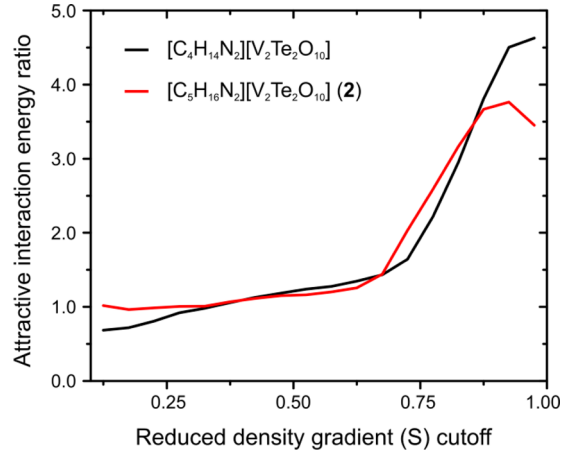

Figure 10. Interaction energy ratios of moderate-density/low-density attractions as a function of reduced density gradient cutoff for $[C_4H_{14}N_2][V_2Te_2O_{10}]$/$[C_5H_{16}N_2][V_2Te_2O_{10}]$ (**2**).

and metal oxide structures can dictate amine exchange reactions,[53] physical phase transitions in gallium phosphates,[54] and vanadium tellurite layer topologies[41] as well as the way in which vanadium selenite SBUs can assemble into structures of different dimensionalities.[42] Additionally, we have demonstrated how tertiary influences can force crystallization in non-centrosymmetric[55−57] or even polar space groups.[40,42,50,58]

1, **2**, and $[C_4H_{14}N_2][V_2Te_2O_{10}]$ can all be synthesized from reaction mixtures that are essentially equivalent, with the only significant difference among the reactions being the structures of the organic amines. This similarity among reaction conditions results in identical vanadium and tellurium speciations across the reactions that result in **1**, **2**, and $[C_4H_{14}N_2][V_2Te_2O_{10}]$. In addition, the relative concentrations of vanadium, tellurium, and the organic amines in these reactions lead to $[V_2Te_2O_{10}]_n^{2n-}$ chains with identical compositions. This suggests that differences between the primary influences are small, resulting in structures containing the same primary building units.

The role of charge-density matching in the formation of **2** and $[C_4H_{14}N_2][V_2Te_2O_{10}]$ can be elucidated through the determination of both the charges and surface areas on the inorganic structures in these two compounds (Table 2). Only small differences in inorganic surface area and charge are observed between the compounds, resulting in nearly identical charge densities on the inorganic structures. These results suggest that charge-density matching is responsible for the similarities between the inorganic SBUs in these compounds.

DOI: 10.1021/ic502753e
Inorg. Chem. 2015, 54, 694−703

Table 2. Surface-Area, Charge, and Charge-Density Results for 1, 2, and $[C_4H_{14}N_2][V_2Te_2O_{10}]$

compound	anion	anion surface area (Å^2)	anion charge	charge density (e Å^{-2})
$[C_6H_{17}N_3][V_2Te_2O_{10}]\cdot H_2O$ (**1**)	$[V_2Te_2O_{10}]_n^{2n-}$	101.52	−1.214	−0.01196
$[C_5H_{16}N_2][V_2Te_2O_{10}]$ (**2**)	$[V_2Te_2O_{10}]_n^{2n-}$	103.37	−1.158	−0.01120
$[C_4H_{14}N_2][V_2Te_2O_{10}]$	$[V_2Te_2O_{10}]_n^{2n-}$	100.65	−1.107	−0.01100

The primary and secondary influences on the formation of **1**, **2**, and $[C_4H_{14}N_2][V_2Te_2O_{10}]$ result in related chains constructed from nearly identical inorganic building units. The differences in $[V_2Te_2O_{10}]_n^{2n-}$ chain metrics must then be the result of weaker tertiary influences involving the organic amines.

However, the organic species, specifically, 1,4-dab and 1,5-dap, have nearly identical physical properties. Using the property calculators in Marvin, version 14.10.20.0,[59] with the pH set to 8, we found that 1,4-dab and 1,5-dap have identical polar surface areas, identical charges on their respective nitrogen atoms, and nearly identical solvent accessible polar atom surface areas. These properties of the organic molecules, which directly influence protonation state and charge density, do not dictate the differences in either chain connectivity or larger 3D packing between **2** and $[C_4H_{14}N_2][V_2Te_2O_{10}]$. Instead, a range of noncovalent interactions within these compounds should account for the differences between compounds.

NCI fingerprints were calculated for $[C_4H_{14}N_2][V_2Te_2O_{10}]$ and **2** in order to probe the role of noncovalent interactions in these structures (Figures 6 and 7, respectively). NCI calculations allow one to locate, quantify, and visualize all noncovalent interactions within a compound. NCI calculations were carried out on these two compounds because (a) they have nearly identical compositions and respective amine structures, only differing by a single $-CH_2-$ group, and (b) they contain both types of chain connectivities. NCI calculations were not carried out on **1** because of the crystallographic disorder in the $[aepH_2]^{2+}$ cations. Using a topological analysis of the electron density and its reduced gradient, the NCI calculations allow for the direct observation of ionic attractions and repulsions, hydrogen bonding, van der Waals attractions, and steric repulsions in these compounds, enabling a much deeper understanding of the forces that govern their formation.

The NCI fingerprints shown in Figures 6 and 7 contain several distinct regions. Attractive interactions correspond to negative sign $(\lambda_2)\rho$ values, with more negative (larger magnitude) values indicating stronger interactions. In contrast, repulsive interactions correspond to positive sign $(\lambda_2)\rho$ values (again, with larger magnitudes indicating stronger interactions, as shown in Figures 6a and 7a). The nature of individual peaks can be determined by isolating and visualizing their respective interactions and isosurfaces, examples of which are shown in Figures 11, S4, and S5. Setting the reduced density gradient cutoff values to either 0.25 or 0.125 resulted in localized interactions whose natures are easily discerned. High-density attractions, corresponding to strong ionic interactions, are observed at sign $(\lambda_2)\rho$ values between approximately −0.25 and −0.05 (Figures 6b and 7b). Moderate- and low-density attractions, including longer ionic interactions, N−H···O and C−H···O hydrogen bonds, and van der Waals attractions, are generally found at sign $(\lambda_2)\rho$ values of −0.04−0 (Figures 6c and 7c). Note that covalent interactions are not shown in these calculations. Differences between the NCI fingerprints of $[C_4H_{14}N_2][V_2Te_2O_{10}]$ and **2** include the relative positions of specific interactions, the number of weak attractions, and the presence of specific repulsive interactions.

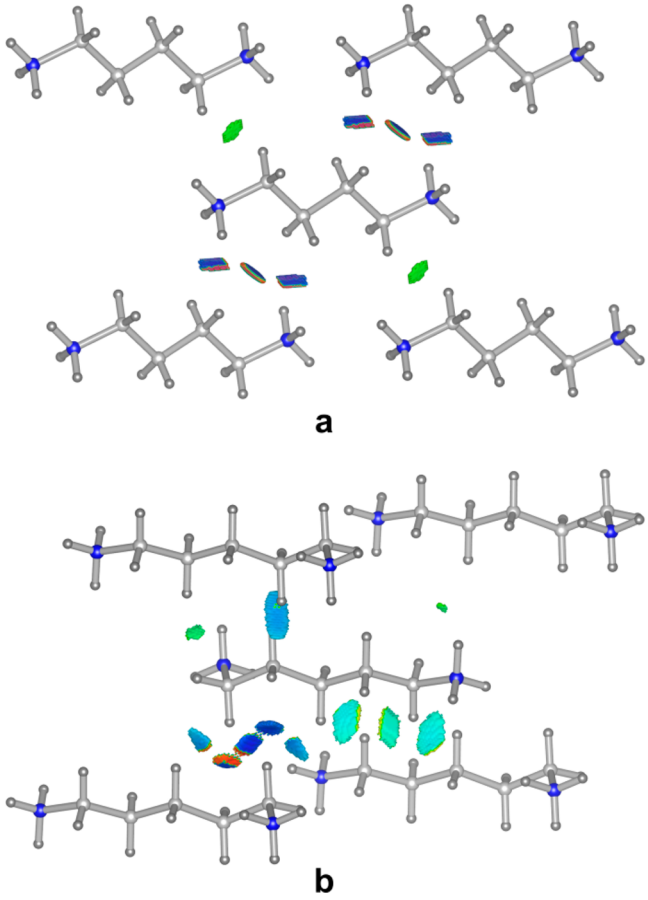

Figure 11. Isosurface plots of intercation van der Waals attractions for (a) $[C_4H_{14}N_2][V_2Te_2O_{10}]$ and (b) **2**. Surface coloring indicates relative strength (sign $(\lambda_2)\rho$), ranging from red (weaker) to blue (stronger).

Because the weaker tertiary influences involving the organic cations are thought to be responsible for the differences in structure between $[C_4H_{14}N_2][V_2Te_2O_{10}]$ and **2**, we focused on the weak attractions and repulsions in our investigation of the noncovalent interactions within these compounds. Specifically, the nature of each type of interaction was identified by plotting the isosurfaces corresponding to each peak in the NCI fingerprints (Figures 6 and 7). Hydrogen-bonding and ionic interactions appear as localized interactions between the donor hydrogen atom and the acceptor atom. Dispersion interactions appear as pancake-shaped regions between the interacting atoms, as shown in Figure 11. Three different groups of noncovalent weak interactions were identified: (i) strong hydrogen bonds and weak ionic interactions, (ii) weak hydrogen bonds and dispersion interactions, and (iii) repulsive interactions. As described above, these can be grouped on the basis of their sign $(\lambda_2)\rho$ values. A quantitative measure of the relative contributions of these different interactions can be obtained by integrating eq 2 for the different regions, as shown in Figures 8 and 9. Although there is no a priori value of s to use as an upper bound when defining $\Omega(NCI)$, $s > 0.6$ results in isosurfaces enclosing large regions that

DOI: 10.1021/ic502753e
Inorg. Chem. 2015, 54, 694−703

do not correspond to typical chemical intuitions of noncovalent interactions because larger, more distributed regions are being included. However, the integrations shown in Figures 8, 9, and 10 are relatively insensitive to the value of s, suggesting that a reasonable upper-bound value was chosen for visualization.

Three differences are observed between $[C_4H_{14}N_2][V_2Te_2O_{10}]$ and **2**. First, the strengths of the moderate- and low-density attractions are higher in compound **2** than in $[C_4H_{14}N_2][V_2Te_2O_{10}]$. As shown in Figure 8, the ratio of the interaction energy of **2** to that of $[C_4H_{14}N_2][V_2Te_2O_{10}]$ is approximately 2. This can be understood qualitatively by considering that $[1,5\text{-dapH}_2]^{2+}$ contains two additional C−H···O hydrogen-bond donors and stronger interactions of the van der Waals type because it contains 14 more electrons than $[1,4\text{-dabH}_2]^{2+}$. The increased number of weak hydrogen-bond donors in $[1,5\text{-dapH}_2]^{2+}$ is by itself unlikely to account for the differences in strengths of these low-density attractions, suggesting that a real difference in van der Waals interactions is responsible. Second, low- and moderate-density repulsive interaction energies are higher in **2** than in $[C_4H_{14}N_2][V_2Te_2O_{10}]$ (Figure 9). Low-density repulsions are defined as interactions for which $0 < \text{sign}(\lambda_2)\rho < 0.2$, whereas moderate-density repulsions are defined as interactions for which $0.2 \leq \text{sign}(\lambda_2)\rho < 0.7$. The global repulsive-interaction-energy ratio mirrors the ratio of low-density repulsions. Third, the strengths of the moderate- and low-density attractions are nearly equal to one another within both $[C_4H_{14}N_2][V_2Te_2O_{10}]$ and **2** (Figure 10). This suggests that in aggregate, the weakest noncovalent interactions play an important role in the determination of the final structure of each compound.

To probe the role of the low-density attractions, interactions between the organic cations and inorganic anions (hydrogen-bonding interactions) and interactions between organic cations (van der Waals forces) were investigated. The $[1,4\text{-dabH}_2]^{2+}$ cations in $[C_4H_{14}N_2][V_2Te_2O_{10}]$ form hydrogen bonds with the $[V_2Te_2O_{10}]_n^{2n-}$ anions, with anion−anion distances of 2.777(4)−3.003(4) Å (Table 3). In contrast, the hydrogen-bonding interactions in **2** differ between the two unique nitrogen sites: N1−H···O distances span a range of 2.760(2)−2.948(2) Å, whereas the N2−H···O interactions have lengths of 2.850(2)−2.928(2) Å (Table 3). These interactions were visualized by isolating their respective NCI isosurface regions, Ω(NCI), as shown in the Supporting Information. Although these N−H···O hydrogen bonds differ in length and strength, the hydrogen-bonding preferences of each ammonium cation are satisfied, with each ammonium site donating three N−H···O bonds to adjacent oxide anions.

Table 3. Selected Hydrogen-Bonding Interactions in 2 and $[C_4H_{14}N_2][V_2Te_2O_{10}]$

	D···A distance (Å)	D−H···A angle (deg)
$[C_5H_{16}N_2][V_2Te_2O_{10}]$ (**2**)		
N1−H1···O3	2.793(2)	154
N1−H2···O2	2.760(2)	160
N1−H3···O6	2.948(2)	159
N2−H14···O1	2.843(2)	159
N2−H15···O10	2.850(2)	173
N2−H16···O7	2.928(2)	170
C2−H6···O3	3.540(2)	129
C3−H8···O3	3.490(2)	150
C5−H12···O7	3.342(2)	149
C5−H13···O6	3.207(2)	127
$[C_4H_{14}N_2][V_2Te_2O_{10}]$		
N1−H1···O5	2.897(4)	144
N1−H2···O4	2.777(4)	154
N1−H3···O3	3.003(4)	138
C1−H5···O4	3.555(4)	140
C1−H5···O1	3.318(4)	124
C2−H6···O4	3.461(4)	147

It is well-known that macroscopic packing differences are observed between even- and odd-numbered chains such as alkanes, alkenediols, and alkenediamines.[60,61] These differences are generally manifested in both symmetric versus asymmetric packing alignments in even- and odd-numbered chains, respectively, and corresponding differences in melting points. Such differences are also observed in **2** and $[C_4H_{14}N_2][V_2Te_2O_{10}]$. The $[1,5\text{-dapH}_2]^{2+}$ cations are staggered in **2**, whereas the $[1,4\text{-dabH}_2]^{2+}$ cations in $[C_4H_{14}N_2][V_2Te_2O_{10}]$ are stacked in regular columns. The staggered nature of the $[1,5\text{-dapH}_2]^{2+}$ cations in **2** is observed in the presence of two distinct orientations (Figure 4). In contrast, the $[1,4\text{-dabH}_2]^{2+}$ cations in $[C_4H_{14}N_2][V_2Te_2O_{10}]$ adopt a single orientation (Figure 5).

The van der Waals interactions in these compounds mirror these packing differences, as shown in Figure 11. The van der Waals interactions in $[C_4H_{14}N_2][V_2Te_2O_{10}]$ are weaker and symmetrical, whereas those in **2** are generally stronger and distinctly asymmetric. The symmetry or asymmetry in the van der Waals forces reflects that the staggered arrangement of $[1,5\text{-dapH}_2]^{2+}$ cations in **2** and the eclipsed $[1,4\text{-dabH}_2]^{2+}$ cations in $[C_4H_{14}N_2][V_2Te_2O_{10}]$ represent the lowest-energy configurations for these compounds. Internal symmetry within the $[1,5\text{-dapH}_2]^{2+}$ cations in **2** is broken, resulting in two unique N sites in **2**. In contrast, $[C_4H_{14}N_2][V_2Te_2O_{10}]$ contains a single nitrogen environment for both ends of the molecule; the two ammonium sites at the ends of the $[1,4\text{-dabH}_2]^{2+}$ cations are symmetrically equivalent. The staggered arrangement of $[1,5\text{-dapH}_2]^{2+}$ cations in **2** results in N1 protruding farther into the space between inorganic chains, forming slightly shorter and stronger hydrogen bonds, whereas N2 remains further away, forming longer and weaker bonds. This results in overall stronger N−H···O hydrogen bonding, which stabilizes the structure further in a fashion analogous to a Peierl's distortion.

The N−H···O hydrogen-bonding interactions in **1**, **2**, and $[C_4H_{14}N_2][V_2Te_2O_{10}]$ are shown in Figure 12. Symmetrical hydrogen-bonding networks are observed in **1** and $[C_4H_{14}N_2][V_2Te_2O_{10}]$, with each ammonium site influencing the orientations of neighboring $[VO_4]$ groups in an analogous fashion. In contrast, a distinct asymmetry is observed in the hydrogen-bonding network in **2**. Both N1 and N2 participate in two hydrogen bonds with the same $[V_2Te_2O_{10}]_n^{2n-}$ chain, to O3 and O6 and to O1 and O7, respectively. All four of these interactions work in concert to cause the $[V(1)O_5]$ and $[V(2)O_4]$ polyhedra to rotate toward one another, causing the distances between the vanadium oxide polyhedra to vary. Notably, the distance between the terminal oxide anions in these polyhedra, O1 and O7, alternates between 4.4680(12) and 6.6069(12) Å, as shown in Figure 2. In addition, the rotation of the $[VO_4]$ and $[VO_5]$ polyhedra in **1**, **2**, and $[C_4H_{14}N_2][V_2Te_2O_{10}]$ directly affects local bonding metrics. For example, rotation of the $[V(1)O_5]$ polyhedra in **2** causes a shortening of the V1−O5 bond with respect to **1** and $[C_4H_{14}N_2][V_2Te_2O_{10}]$, whereas rotation of the $[V(2)O_4]$ tetrahedra in the opposite direction moves O6 away from Te1 (Figure 2). The rotation of $[V(1)O_5]$ in **2** also results in shorter V1−Te1 and V1−Te2

DOI: 10.1021/ic502753e
Inorg. Chem. 2015, 54, 694−703

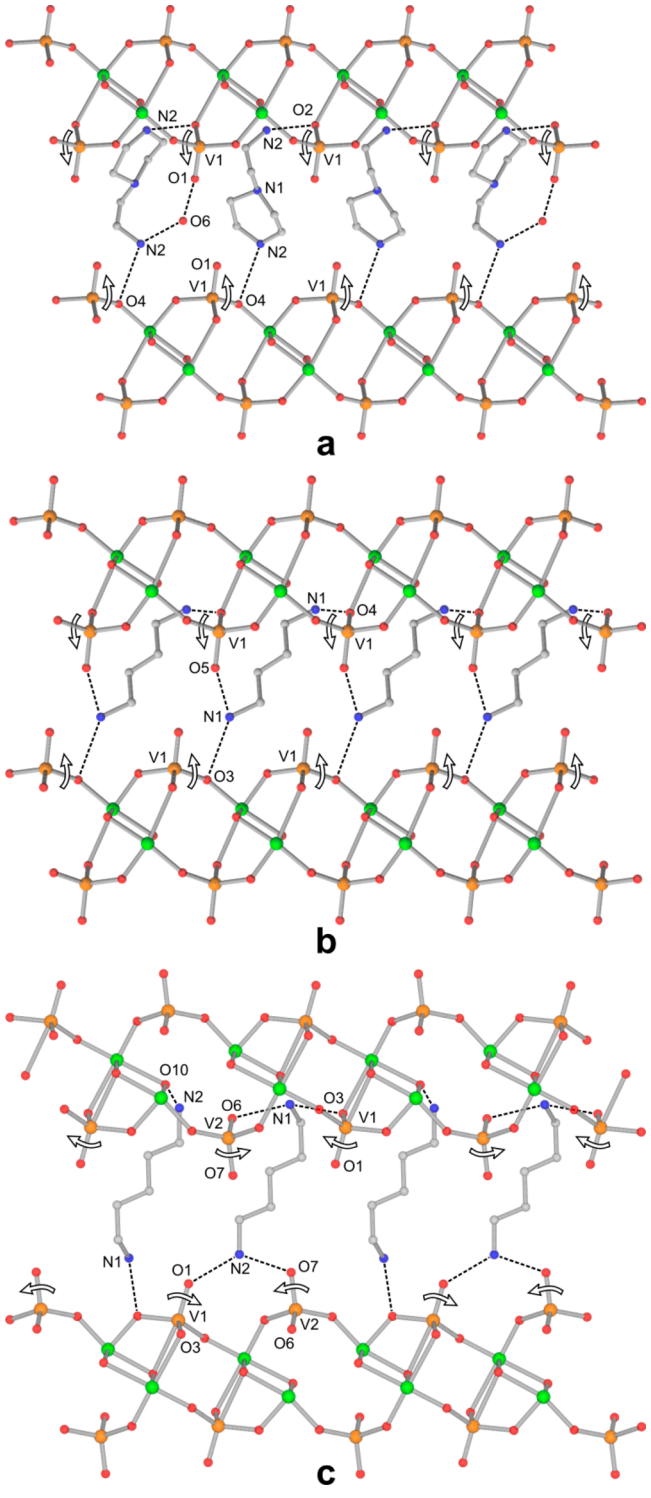

Figure 12. Hydrogen-bonding interactions in (a) **1**, (b) $[C_4H_{14}N_2][V_2Te_2O_{10}]$, and (c) **2**. Orange, green, red, blue, and white spheres represent vanadium, tellurium, oxygen, nitrogen, and carbon, respectively. Hydrogen atoms have been omitted for clarity.

distances of 3.341(2) and 3.444(2) Å, respectively. These distances in $[C_4H_{14}N_2][V_2Te_2O_{10}]$ are 3.391(4) and 3.723(4) Å, respectively. Repulsions associated with the shorter V−Te distances in **2** are observed in the NCI fingerprints; the doublet labeled with an orange triangle in Figure 7a corresponds to this repulsion.

Differences in the low-density attractions between organic cations result in divergent packing motifs for the $[1,4\text{-dabH}_2]^{2+}$ cations in $[C_4H_{14}N_2][V_2Te_2O_{10}]$ and the $[1,5\text{-dapH}_2]^{2+}$ cations in **2**. This, in turn, forces a reorganization of the N−H···O hydrogen bonds, which then causes the structural differences in the $[V_2Te_2O_{10}]_n^{2n-}$ chains.

CONCLUSIONS

The formation of compounds such as **1**, **2**, and $[C_4H_{14}N_2][V_2Te_2O_{10}]$ is influenced by a number of sources, all of which work to minimize free energy under the experimental conditions of the reaction. Many types of interactions, both strong and weak, exert some influence over the resulting structure. NCI calculations enable one to locate, quantify, and visualize these weak interactions and to elucidate the way in which they influence structure as well as being an exceptionally important tool in understanding the formation of these complex materials. This computational technique allows us to ascribe the differences in $[V_2Te_2O_{10}]_n^{2n-}$ chain connectivities to specific intermolecular interactions. Specifically, low-density intermolecular attractions (C−H···O hydrogen bonds and van der Waals forces) were found to exert considerable influence over the resulting structures.

ASSOCIATED CONTENT

Supporting Information

A Mathematica file for creating NCI isosurfaces and integrating eq 1 can be directly accessed at http://triceratops.brynmawr.edu:8080/dspace/handle/10066/15138. Tables of bond valence sums, iterative Hirshfeld partial atomic charges and attractive and repulsive interaction energy ratios, CRITIC2 input files, figures of experimental and simulated powder X-ray diffraction patterns for **1** and **2**, the crystallographic disorder mechanism for the $[aepH_2]^{2+}$ cations in **1**, NCI isosurfaces as a function of reduced density gradient cutoff for **2** and $[C_4H_{14}N_2][V_2Te_2O_{10}]$, NCI isosurfaces for N−H···O interactions in **2** and $[C_4H_{14}N_2][V_2Te_2O_{10}]$, and X-ray crystallographic information files (CIF) for $[C_6H_{17}N_3][V_2Te_2O_{10}]\cdot H_2O$ (**1**) and $[C_5H_{16}N_2][V_2Te_2O_{10}]$ (**2**). This material is available free of charge via the Internet at http://pubs.acs.org.

AUTHOR INFORMATION

Corresponding Author

*E-mail: anorquis@haverford.edu.

Notes

The authors declare no competing financial interest.

ACKNOWLEDGMENTS

The authors thank Dr. Alberto Otero-de-la-Roza and Dr. Julia Contreras-García for providing source code and assistance in troubleshooting our NCI calculations and Joe Cammisa for technical help. The authors acknowledge support from the NSF (Award DMR-1307801), the Henry Dreyfus Teacher-Scholar Awards Program, and grants to Haverford College from the HHMI Undergraduate Science Education Program. M.Z. acknowledges support for the purchase of a diffractometer from the NSF (Grant 0087210), the Ohio Board of Regents (Grant CAP-491), and Youngstown State University. G.M.F. acknowledges the NSF (Award CHE-1039689) for funding Illinois State University's X-ray diffractometer. This research used the computational resources of the National Energy Research Scientific Computing Center (NERSC), which is

DOI: 10.1021/ic502753e
Inorg. Chem. 2015, 54, 694−703

supported by the Office of Science of the U.S. Department of Energy under Contract DE-AC02-05CH11231.

REFERENCES

(1) Park, K. S.; Ni, Z.; Cote, A. P.; Choi, J. Y.; Huang, R.; Uribe-Romo, F. J.; Chae, H. K.; O'Keeffe, M.; Yaghi, O. M. *Proc. Natl. Acad. Sci. U.S.A.* **2006**, *103*, 10186−10191.
(2) Yaghi, O. M.; O'Keeffe, M.; Ockwig, N. W.; Chae, H. K.; Eddaoudi, M.; Kim, J. *Nature* **2003**, *423*, 705−714.
(3) Li, H.; Eddaoudi, M.; O'Keeffe, M.; Yaghi, M. *Nature* **1999**, *402*, 276−279.
(4) Kusukawa, T.; Fujita, M. *J. Am. Chem. Soc.* **1999**, *121*, 1397−1398.
(5) Fujita, M.; Su, S.-Y.; Kusukawa, T.; Funaki, H.; Ogura, K.; Yamaguchi, K. *Angew. Chem., Int. Ed.* **1998**, *37*, 2082−2085.
(6) Baumann, F.; Livoreil, A.; Kaim, W.; Sauvage, J.-P. *Chem. Commun.* **1997**, 35−36.
(7) Amabilino, D. B.; Dietrich-Buchecker, C. O.; Livoreil, A.; Perez-Garcia, L.; Sauvage, J.-P.; Stoddart, J. F. *J. Am. Chem. Soc.* **1996**, *118*, 3905−3913.
(8) Cheetham, A. K.; Rao, C. N. R.; Feller, R. K. *Chem. Commun.* **2006**, 4780−4795.
(9) Cheetham, A. K.; Ferey, G.; Loiseau, T. *Angew. Chem., Int. Ed.* **1999**, *38*, 3268−3292.
(10) Desiraju, G. R. *Chem. Commun.* **2005**, 2995−3001.
(11) Muthuraman, M.; Masse, R.; Nicoud, J.-F.; Desiraju, G. R. *Chem. Mater.* **2001**, *13*, 1473−1479.
(12) Desiraju, G. R. *Acc. Chem. Res.* **1996**, *29*, 441−449.
(13) Desiraju, G. R. *Acc. Chem. Res.* **1991**, *24*, 290−296.
(14) Johnson, E. R.; Keinan, S.; Mori-Sanchez, P.; Contreras-García, J.; Cohen, A. J.; Yang, W. *J. Am. Chem. Soc.* **2010**, *132*, 6498−6506.
(15) Otero-de-la-Roza, A.; Johnson, E. R.; Contreras-García, J. *Phys. Chem. Chem. Phys.* **2012**, *14*, 12165−12172.
(16) Contreras-García, J.; Johnson, E. R.; Keinan, S.; Chaudret, R.; Piquemal, J.-P.; Beratan, D. N.; Yang, W. *J. Chem. Theory Comput.* **2011**, *7*, 625−632.
(17) Yang, J.; Waller, M. P. *J. Comput. Chem.* **2013**, *34*, 466−470.
(18) Badri, Z.; Bouzkova, K.; Foroutan-Nejad, C.; Marek, R. *Cryst. Growth Des.* **2014**, *14*, 2763−2772.
(19) Dale, S. G.; Otero-de-la-Roza, A.; Johnson, E. R. *Phys. Chem. Chem. Phys.* **2014**, *16*, 14584−14593.
(20) Galvelis, R.; Slater, B.; Chaudret, R.; Creton, B.; Nieto-Draghi, C.; Mellot-Draznieks, C. *CrystEngComm* **2013**, *15*, 9603−9612.
(21) Chang, K. B.; Hubbard, D. J.; Zeller, M.; Schrier, J.; Norquist, A. J. *Inorg. Chem.* **2010**, *49*, 5167−5172.
(22) *APEX2*; Bruker AXS Inc.: Madison, WI, 2009.
(23) Altomare, A.; Cascarano, G.; Giacovazzo, C.; Guagliardi, A. *J. Appl. Crystallogr.* **1993**, *26*, 343−350.
(24) Betteridge, P. W.; Carruthers, J. R.; Cooper, R. I.; Prout, K.; Watkin, D. J. *J. Appl. Crystallogr.* **2003**, *36*, 1487.
(25) Dowty, E.; *ATOMS*, version 6.0; Shape Software: Kingsport, TN, 2002.
(26) Brown, I. D.; Altermatt, D. *Acta Crystallogr., Sect. B* **1985**, *41*, 244−247.
(27) Brese, N. E.; O'Keeffe, M. *Acta Crystallogr., Sect. B* **1991**, *47*, 192−197.
(28) Gonze, X.; Beuken, J. M.; Caracas, R.; Detraux, F.; Fuchs, M.; Rignanese, G. M.; Sindic, L.; Verstraete, M.; Zerah, G.; Jollet, F.; Torrent, M.; Roy, A.; Mikami, M.; Ghosez, P.; Raty, J. Y.; Allan, D. C. *Comput. Mater. Sci.* **2002**, *25*, 478−492.
(29) Gonze, X.; Amadon, B.; Anglade, P. M.; Beuken, J. M.; Bottin, F.; Boulanger, P.; Bruneval, F.; Caliste, D.; Caracas, R.; Cote, M.; Deutsch, T.; Genovese, L.; Ghosez, P.; Giantomassi, M.; Goedecker, S.; Hamann, D. R.; Hermet, P.; Jollet, F.; Jomard, G.; Leroux, S.; Mancini, M.; Mazevet, S.; Oliveira, M. J. T.; Onida, G.; Pouillon, Y.; Rangel, T.; Rignanese, G. M.; Sangalli, D.; Shaltaf, R.; Torrent, M.; Verstraete, M. J.; Zerah, G.; Zwanziger, J. W. *Comput. Phys. Commun.* **2009**, *180*, 2582−2615.
(30) Momma, K.; Izumi, F. *J. Appl. Crystallogr.* **2008**, *41*, 653−658.
(31) Otero-de-la-Roza, A.; Blanco, M. A.; Pendas, A. M.; Luana, V. *Comput. Phys. Commun.* **2009**, *180*, 157−166.
(32) Otero-de-la-Roza, A.; Johnson, E. R.; Luana, V. *Comput. Phys. Commun.* **2014**, *185*, 1007−1018.
(33) Contreras-García, J.; Yang, W.; Johnson, E. R. *J. Phys. Chem. A* **2011**, *115*, 12983−12990.
(34) Schindler, M.; Hawthorne, F. C.; Baur, W. H. *Chem. Mater.* **2000**, *12*, 1248−1259.
(35) Heier, K. R.; Norquist, A. J.; Wilson, C. G.; Stern, C. L.; Poeppelmeier, K. R. *Inorg. Chem.* **1998**, *37*, 76−80.
(36) Norquist, A. J.; Doran, M. B.; O'Hare, D. *Inorg. Chem.* **2005**, *44*, 3837−3843.
(37) Casalongue, H. S.; Choyke, S. J.; Narducci Sarjeant, A.; Schrier, J.; Norquist, A. J. *J. Solid State Chem.* **2009**, *182*, 1297−1303.
(38) Hubbard, D. J.; Johnston, A. R.; Casalongue, H. S.; Narducci Sarjeant, A.; Norquist, A. J. *Inorg. Chem.* **2008**, *47*, 8518−8525.
(39) Kaufman, E. A.; Zeller, M.; Norquist, A. J. *Cryst. Growth Des.* **2010**, *10*, 4656−4661.
(40) Smith, M. D.; Blau, S. M.; Chang, K. B.; Tran, T. T.; Zeller, M.; Halasyamani, P. S.; Schrier, J.; Norquist, A. J. *J. Solid State Chem.* **2012**, *195*, 86−93.
(41) Smith, M. D.; Blau, S. M.; Chang, K. B.; Zeller, M.; Schrier, J.; Norquist, A. J. *Cryst. Growth Des.* **2011**, *11*, 4213−4219.
(42) Olshansky, J. H.; Thao Tran, T.; Hernandez, K. J.; Zeller, M.; Halasyamani, P. S.; Schrier, J.; Norquist, A. J. *Inorg. Chem.* **2012**, *51*, 11040−11048.
(43) Halasyamani, P.; Willis, M. J.; Stern, C. L.; Lundquist, P. M.; Wong, G. K.; Poeppelmeier, K. R. *Inorg. Chem.* **1996**, *35*, 1367−1371.
(44) Norquist, A. J.; Heier, K. R.; Stern, C. L.; Poeppelmeier, K. R. *Inorg. Chem.* **1998**, *37*, 6495−6501.
(45) Norquist, A. J.; Doran, M. B.; Thomas, P. M.; O'Hare, D. *Dalton Trans.* **2003**, 1168−1175.
(46) Thomas, P. M.; Norquist, A. J.; Doran, M. B.; O'Hare, D. *J. Mater. Chem.* **2003**, *13*, 88−92.
(47) Nelson, J. H.; Johnston, A. R.; Narducci Sarjeant, A.; Norquist, A. J. *Solid State Sci.* **2007**, *9*, 472−484.
(48) Veltman, T. R.; Stover, A. K.; Narducci Sarjeant, A.; Ok, K. M.; Halasyamani, P. S.; Norquist, A. J. *Inorg. Chem.* **2006**, *45*, 5529−5537.
(49) Stover, A. K.; Gutnick, J. R.; Narducci Sarjeant, A.; Norquist, A. J. *Inorg. Chem.* **2007**, *46*, 4389−4391.
(50) Koffer, J. H.; Olshansky, J. H.; Smith, M. D.; Hernandez, K. J.; Zeller, M.; Ferrence, G. M.; Schrier, J.; Norquist, A. J. *Cryst. Growth Des.* **2013**, *13*, 4504−4511.
(51) Ferey, G. *Chem. Mater.* **2001**, *13*, 3084−3098.
(52) Ferey, G. *J. Fluorine Chem.* **1995**, *72*, 187−193.
(53) Chang, K. B.; Smith, M. D.; Blau, S. M.; Glor, E. C.; Zeller, M.; Schrier, J.; Norquist, A. J. *Cryst. Growth Des.* **2013**, *13*, 2190−2197.
(54) Olshansky, J. H.; Blau, S. M.; Zeller, M.; Schrier, J.; Norquist, A. J. *Cryst. Growth Des.* **2011**, *11*, 3065−3071.
(55) Gutnick, J. R.; Muller, E. A.; Narducci Sarjeant, A.; Norquist, A. J. *Inorg. Chem.* **2004**, *43*, 6528−6530.
(56) Muller, E. A.; Cannon, R. J.; Narducci Sarjeant, A.; Ok, K. M.; Halasyamani, P. S.; Norquist, A. J. *Cryst. Growth Des.* **2005**, *5*, 1913−1917.
(57) Choyke, S. J.; Blau, S. M.; Larner, A. A.; Narducci Sarjeant, A.; Yeon, J.; Halasyamani, P. S.; Norquist, A. J. *Inorg. Chem.* **2009**, *48*, 11277−11282.
(58) Glor, E. C.; Blau, S. M.; Yeon, J.; Zeller, M.; Shiv Halasyamani, P.; Schrier, J.; Norquist, A. J. *J. Solid State Chem.* **2011**, *184*, 1445−1450.
(59) *Marvin*, version 14.10.20.0; ChemAxon: Budapest, Hungary, 2014. http://www.chemaxon.com (accessed December 17, 2014).
(60) Boese, R.; Weiss, H.-C.; Blaser, D. *Angew. Chem., Int. Ed.* **1999**, *38*, 988−992.
(61) Thalladi, V. R.; Boese, R.; Weiss, H.-C. *Angew. Chem., Int. Ed.* **2000**, *39*, 918−922.

DOI: 10.1021/ic502753e
Inorg. Chem. 2015, 54, 694−703